Engineering 7 (2021) 1424–1433

Contents lists available at ScienceDirect

Engineering

journal homepage: www.elsevier.com/locate/eng

Research
New Technology of Tumor Diagnosis and Treatment—Article

Effects of Three-Dimensional Platform Stiffness and Layer Dimensions on Separation of Carcinoma Cells

W.G. Zhang, Z.Y. Liu, S.W. Pang *

Department of Electrical Engineering, Center for Biosystems, Neuroscience, and Nanotechnology, City University of Hong Kong, Hong Kong 999077, China

ARTICLE INFO

Article history:
Received 6 May 2020
Revised 23 July 2020
Accepted 1 September 2020
Available online 5 November 2020

Keywords:
Cell separation
Cell migration
Nasopharyngeal carcinoma (NPC)
3D scaffold platform

ABSTRACT

Cancer cell separation is highly desirable for cancer diagnosis and therapy. Besides biochemical methods, engineered platforms are effective alternatives for sorting carcinoma cells from normal cells based on their unique properties in responding to the physical changes of the surrounding microenvironment. In this work, three-dimensional (3D) biomimetic scaffold platforms were developed to separate nasopharyngeal carcinoma 43 (NPC43) cells from immortalized nasopharyngeal epithelial 460 (NP460) cells based on precisely controlled design parameters including stiffness, number of layers, and structural layout. The migration characteristics of NPC43 and NP460 cells on the scaffold platforms revealed that NPC43 cells could squeeze into 10 μm wide, 15 μm deep trenches while NP460 cells could not. The different migration behavior was mainly due to cells having different interactions with the surrounding microenvironment. NPC43 cells had filopodia-like protrusions, while NP460 cells exhibited a sheet-like morphology. Using these 3D biomimetic platforms, 89% separation efficiency of NPC43 cells from NP460 cells was achieved on stiffer two-layer scaffold platforms with a 40/10 μm ridge/trench (R/T) grating on the top layer and a 20/10 μm R/T grid on the bottom layer. Moreover, the separation efficiency was further increased to 93% by adding an active conditioned medium (ACM) that caused the cells to have higher motility and deformability. These results demonstrate the capability to apply biomimetic engineered platforms with appropriate designs to separate cancer cells from normal cells for potential cancer diagnosis and treatment.

1. Introduction

A tumor is a complex heterogeneous tissue that consists of extracellular matrix (ECM) filled with cancer cells and non-cancer stromal cells. Different kinds of stromal cells including fibroblasts, immune cells, macrophages, and endothelial cells co-occupy and interact with the surrounding cancer cells [1–5]. The ability to separate cancer cells from a heterogeneous cell population will be desirable in cancer diagnostics, monitoring, and therapeutics. Biomarkers are typically used to identify different cell types; for example, complementary fluorophore-conjugated antibodies are bonded to target cells so that the target cells can be identified by fluorescent detectors [6–9]. Alternatively, by combining antibody-conjugated magnetic beads to specific proteins on the cells of interest, labeled cells can be sorted by exerting a magnetic force on the beads via an applied external magnetic field [10–13]. Cells are also picked manually for single-cell isolation [14–16]. Micro-manipulators and micropipettes can be used to pick up specific cells under an inverted microscope. In addition, microfluidic systems have been developed for cell sorting and have the advantages of precise flow control, device minimization, and low sample consumption [17–20]. In addition to biomarkers, cell properties including cell size [21–23], shape [24–26], deformability [27,28], density [29], polarizability [30,31], and reflective index [32,33] have been utilized to separate cells in microfluidic systems with the help of microfluidic force. For example, funnel-shaped microstructures in microfluidic systems were used to block larger or more rigid cells, while smaller or more deformable cells could pass through under oscillatory flow [34,35]. Although cells can be separated with high efficiency [36], they often require external setups or forces such as biomarkers, antibodies, a magnetic field, or microfluidic flow, which make the process more complicated and expensive.

Aside from methods that utilize external biochemical agents or external magnetic or microfluidic forces to separate cells, other

* Corresponding author.
E-mail address: pang@cityu.edu.hk (S.W. Pang).

https://doi.org/10.1016/j.eng.2020.09.010

methods take advantage of cell interaction behaviors on designed platforms. Previously, our group studied a one-layer platform with different designs for cell migration and separation [37,38]. While one-layer platforms were found to be effective in providing guidance for cell migration, they were not able to separate cancer cells from normal cells. Therefore, three-dimensional (3D) platforms were developed to provide the capability for cell separation. 3D platforms also provide a better representation of the ECM in tissues, as the ECM is 3D in real life. In combination with the microfluidic channels in 3D platforms, isolated cells can be collected separately for further studies. Thus, in this study, the focus was on the separation of nasopharyngeal carcinoma (NPC) cells from nasopharyngeal epithelial (NP) cells by using controllable 3D scaffold platforms. NPC is recognized as a highly invasive and metastatic cancer, and patients often do not exhibit clear symptoms in the early stage [39–41]. Unlike other types of cancers, NPC is strongly associated with Epstein–Barr virus (EBV). However, the EBV episomes often diminish when NPC cells are cultured *in vitro* [42,43]. Recently, a series of stable NPC cell lines was successfully established [44]. Therefore, it is important to carry out an *in vitro* study of NPC cells with regard to their migration behaviors, and to develop platforms for cancer cell separation without chemical additions or external force.

In this work, 3D scaffold platforms were designed and developed to utilize the inherent unique NPC cell morphology, migration characteristics, and different interactions with the surrounding microenvironment in order to separate NPC43 cells from immortalized NP460 cells. As the size of NP460 and NPC43 cells is approximately 15 μm, when they were cultured on one-layer grating platforms with 10 μm wide and 15 μm deep trenches, these cells could hardly squeeze into the 10 μm wide trenches, since the trench width was narrower than the cell size. Thus, by designing 3D scaffold platforms with different dimensions, layouts, and material properties, NP460 and NPC43 cells with similar size could be separated based on whether or not they could migrate into the narrow trenches. With the proper platform stiffness, multi-layer layouts, and layer dimensions, NPC43 cells had an 85% probability of squeezing into the 10 μm wide trenches, while NP460 cells only had a 10% chance of being in the narrow trenches. In addition, when NPC43 cells had higher motility due to being stimulated by an active conditioned medium (ACM), they showed a high probability of squeezing into the 10 μm wide trenches, resulting in a higher cell-separation efficiency.

2. Materials and methods

2.1. Fabrication of engineered scaffold platform

One-layer and two-layer scaffold platforms were fabricated with a biocompatible elastomer polydimethylsiloxane (PDMS). A one-layer platform was formed by a replica molding technique, as reported previously [37,38]. The process flow for the two-layer platform is demonstrated in Fig. 1; this consisted of fabricating the top and bottom layers separately and stacking the two layers together by reversal imprinting after treating the layers with an oxygen (O_2) plasma. The bottom layer was prepared identically as a one-layer scaffold platform, as shown in Fig. 1(a). After coating the Si grating mold with an anti-sticking layer of trichloro(1*H*,1*H*,2*H*,2*H*-perfluorooctyl)silane (FOTS), the PDMS mixture was cast on the mold and cured on a hotplate at 80 °C for 6 h. The stiffness of the PDMS was modified by using a different prepolymer base and curing agent (Dow Corning Sylgard 184 kit, USA) with three mix ratios of 5:1, 10:1, and 30:1 (w/w). The stiffness was characterized using a nanoindenter (Hysitron TI 700 Ubi, USA). The top layer was fabricated by reversal imprinting a PDMS layer using a Si grating mold coated with FOTS (surface energy: (71 ± 3) $mN \cdot m^{-1}$) and a Si substrate coated with another anti-stacking layer with a 4:1 mass mixture of 3-methacryloxypropyltrichlorosilane (MOPTS) and FOTS (surface energy : (23 ± 3) $mN \cdot m^{-1}$). Both the top and bottom layers were then treated with an O_2 plasma for 1 min with an O_2 flow rate of 20 sccm (1 sccm = 1 $cm^3 \cdot min^{-1}$) a chamber pressure of 80 mTorr (1 mTorr = 0.133 Pa), and a radio frequency (RF) power of 60 W. The two grating layers were bonded together by stacking them perpendicularly to each other. After baking at 80 °C for 10 min, t he two-layer scaffold platform was peeled off from the Si substrate.

2.2. Cell culture

Both the NP460 and NPC43 cells were obtained from the S. W. Tsao team developed by Lin et al. [44]. NP460 cells were cultured in the medium using a 1:1 mixture of EpiLife medium (Gibco, USA) fully supplemented with 1% EpiLife defined growth supplement (EDGS; Gibco) and a defined Keratinocyte-serum free medium (1×; Gibco) medium fully supplemented with 0.2% defined Keratinocyte growth supplement (Gibco). NPC43 cells were maintained in Roswell Park Memorial Institute (RPMI) 1640 medium (1×; Gibco) with 10% fetal bovine serum (FBS) and 0.2% of 2 $mmol \cdot L^{-1}$ rock inhibitor Y-27632 (25 mg; ENZO, Switzerland). Both the NP460 and NPC43 cell culture mediums were mixed with 1% antibiotic antimycotic (Gibco; 100 units (U) per milliliter penicillin G sodium, 100 $mg \cdot mL^{-1}$ streptomycin, and 0.25 $mg \cdot mL^{-1}$ amphotericin B) to avoid contamination. The mediums were changed every two days and cells were passed every five days.

2.3. Time-lapse and immunofluorescence imaging

The 3D scaffold platforms were bonded on 35 mm glass-bottom confocal dishes for imaging. Before cell seeding, the platforms were treated with an O_2 plasma for 1 min with an O_2 flow rate of 20 sccm, chamber pressure of 80 mTorr, and RF power of 60 W to create a hydrophilic surface to enhance the attachment of cells onto the platforms. After the surface treatment, cells were immediately seeded at a density of 7.0×10^4 and 1.1×10^5 $cells \cdot mL^{-1}$ with a volume of 2 mL onto the one-layer and two-layer platforms, respectively, and put in the incubator for 6 h. After that, the medium was replaced by the 1:1 mixture of cell culture medium and carbon dioxide (CO_2)-independent medium 18045–088 (Invitrogen, USA), which was supplemented with 10% FBS, 1% penicillin streptomycin (10 000 $U \cdot mL^{-1}$; Gibco), and 1% GlutaMAX (100×; Gibco) to provide an environment without the need for a CO_2-filled incubator. A Nikon Eclipse Ni-E upright motorized microscope (Japan) was then used to take time-lapse images every 5 min for 15 h. Live cell immunofluorescence images were captured by the same microscope with the function of fluorescein isothiocyanate and tetraethyl rhodamine isothiocyanate imaging.

2.4. Data analysis

Cell migration speed and trajectory were tracked by the National Institutes of Health (NIH) ImageJ (version 1.50i; USA) packaged with a Manual Tracking plugin (USA). Cell morphology analysis was accomplished by the measure function in ImageJ after circling the cell shape; and the cell area, perimeter, and ellipse-fitted long axis and short axis were calculated. Cells that died, divided, or came into contact with other cells during the time-lapse imaging were excluded from the analysis.

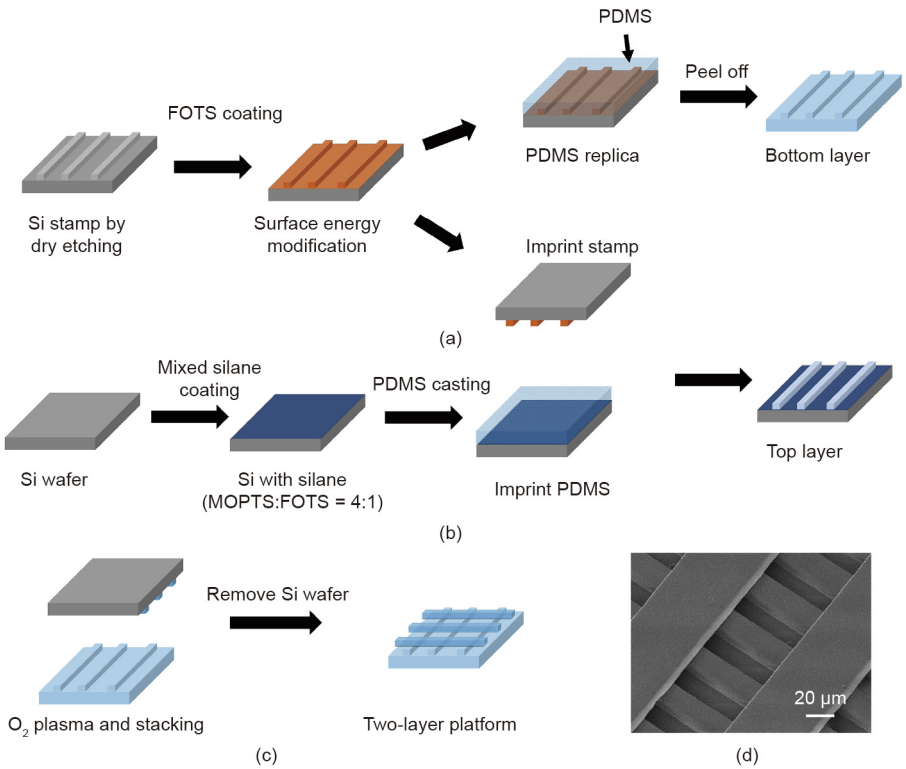

Fig. 1. Fabrication of a two-layer platform. (a) Si mold coated with FOTS for pattern replication on PDMS. (b) Si wafer coated with mixed silane with patterned PDMS formed by imprinting. (c) Two-layer platform formed by stacking two layers of patterned PDMS together after O_2 plasma treatment. (d) Micrograph of the fabricated two-layer platform. FOTS: trichloro(1*H*,1*H*,2*H*,2*H*-perfluorooctyl)silane; MOPTS: 3-methacryloxypropyltrichlorosilane.

Cell roundness (R) was calculated as follows:

$$R = \frac{A}{\pi \times [C/(2\pi)]^2} \quad (1)$$

where A is the projected area and C is the perimeter of the cell.

To calculate the aspect ratio of the cell shape, an ellipse was overlaid on the cell with a short axis a and a long axis b, so that the aspect ratio was obtained by b/a. Statistical difference between groups was analyzed using a one-way analysis of variance (ANOVA) test with a significant level at $p < 0.05$. All the results are presented as mean ± standard error of the mean (SEM).

Cell-separation efficiency was defined by using the probability of NPC43 cells in the top-layer trenches or bottom grids divided by the probability of NPC43 and NP460 cells in that specific location.

2.5. Scanning electron microscopy

Cells on platforms were rinsed with 10× phosphate buffer saline (PBS) two times (5 min each), and then fixed by 4% paraformaldehyde for 15 min. Dehydration of cells was then performed by gradually increasing the ethanol concentration from 30%, 50%, 70%, 80%, 90%, 95% to 100%; the cells were then kept in a critical point dryer for 3 h. The dried samples were then coated with a thin layer of Au to avoid charging and placed in a scanning electron microscope SU5000 (Hitachi, Japan) for imaging.

3. Results and discussion

3.1. Cell separation on one-layer platforms

3.1.1. Effects of platform stiffness

Substrate stiffness has been shown to influence cell behaviors such as migration speed, morphology, and proliferation [45–48]. In this work, one-layer grating platforms with trenches 10 μm wide and 15 μm deep were used to investigate the effects of platform stiffness on the probability of NP460 and NPC43 cells squeezing into the narrow trenches. The probability of cells squeezing into the 10 μm wide trenches is defined as the number of cells in the narrow trenches divided by the total cell number. Cells that had divided, died, or came into contact with other cells were excluded from the statistical analysis to avoid other effects due to cell status changes. Different platform stiffnesses were obtained by different PDMS base:agent mix ratios. The measured Young's modulus shown in Fig. 2(a) indicates that a higher mix ratio resulted in a smaller Young's modulus with softer platforms.

NP460 and NPC43 cells were seeded on the platforms separately and then incubated for 6 h followed by 15 h of time-lapse imaging. Fig. 2(b) shows that almost no NP460 cells could squeeze into the 10 μm wide trenches regardless of the platform stiffness, whereas 23% of the NPC43 cells were found in the narrow trenches on stiffer platforms. On stiffer platforms, NPC43 cells could be separated from NP460 cells. The results shown in Fig. 2(b) indicate that the softer platform fabricated using a 30:1 PDMS base:agent mix ratio could not be used to separate NPC43 cells from NP460 cells. Thus, relatively stiffer platforms that were fabricated using the 5:1 and 10:1 PDMS base:agent mix ratios were chosen for further investigation and characterization. The micrographs in Fig. 2(c) show the different morphologies of NP460 and NPC43 cells on the platforms with PDMS base:agent mix ratios of 5:1 and 10:1. Typically, NP460 cells had larger cell bodies that spread in all directions. On the other hand, NPC43 cells were smaller; they aligned along the grating orientation on stiffer platforms but were more rounded on softer platforms. Cell roundness was calculated and is shown in Fig. 2(d) with a roundness of 1 for a circle. NP460 cell roundness had no significant dependence on platform stiffness, whereas NPC43 cells became more elongated on stiffer platforms

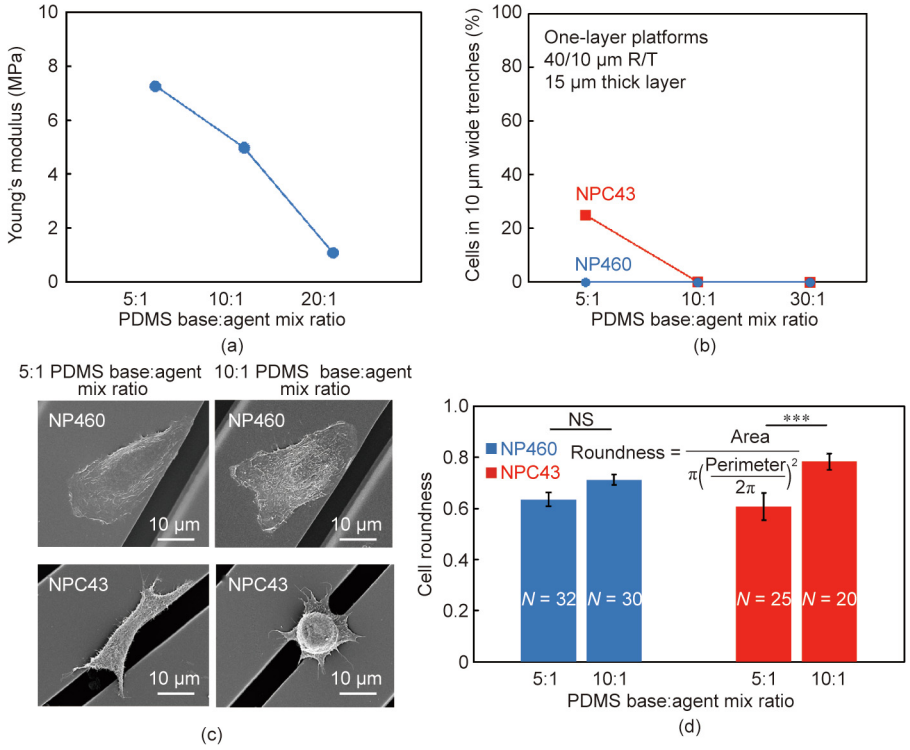

Fig. 2. (a) Measured Young's modulus of PDMS with different base:agent mix ratios (error bar ± 12 kPa). (b) Probabilities of NP460 and NPC43 cell migration into 10 μm wide trenches on one-layer platforms with different stiffnesses (error bars within 1%). (c) Micrographs and (d) cell morphology of NP460 and NPC43 cells on one-layer platforms with different stiffnesses. The trenches were 10 μm wide and 15 μm deep. Cell numbers (N) > 20. R/T: ridge/trench; NS: not significant. ***: $p < 0.001$.

and could have a higher probability of squeezing into the narrow trenches.

3.1.2. Effects of pattern shape and layout

Cell contact area in a tight opening can determine cell migration path, direction, or cell shape deformation. Therefore, one-layer platforms with four different pore shapes with the same opening area, including a circle, hexagon, square, and triangle, were created to examine how NPC43 cells moved around pores with different shapes, as shown schematically in Fig. 3(a). The diameter of the 15 μm deep circular pore was 18 μm, which was roughly equivalent to the cell size; thus, all four shapes were designed with the same area of about 256 μm^2. After cell seeding for 7 h, the cells were still rounded and could not completely fill the entire pore. Therefore, the degree of pore filling, which was defined by dividing the cell area by the pore area, was used to quantify the change of cell size in the pores. As shown in Fig. 3(a), the NPC43 cells initially had a different degree of filling in pores with different shapes, but could eventually fill the entire pores of the different shapes after 22 h. This indicated that the NPC43 cells could extend their bodies to fill in the tight openings of the different shapes.

Because of the abovementioned properties, the patterns on the one-layer platform were modified from a grating to a grid so that more contact area was formed at the grid intersections, which could allow more NPC43 cells to get into the 10 μm wide trenches for cell separation. The migration trajectories of NPC43 cells on the one-layer platforms with a grating and a grid have been plotted in Fig. 3(b). The figure shows that the grating pattern guided the cells to migrate along its orientation with more elongated morphology, while the grid pattern localized the cells at the intersections with more rounded morphology. The probability of NPC43 cells squeezing into the 10 μm wide trenches was higher on platforms with a grid, as shown in Fig. 3(c), which implies that a higher separation efficiency of NPC43 cells from NP460 cells was achieved with the grid design on the bottom layer.

3.2. Cell separation on two-layer platforms

3.2.1. Effects of platform stiffness

Multi-layer 3D platforms were developed for cell separation, as shown in Fig. 4(a). Two-layer scaffold platforms were used to mimic the ECM in tissue, which consists of a 3D microenvironment, to enable the cells to migrate. The dimensions of the patterns on both the top and bottom layers were a 40/10 μm ridge/trench (R/T) grating that was 15 μm deep.

As shown in Fig. 4(a), the NP460 and NCP43 cells had different morphologies on the platforms. The NP460 cell developed sheet-like lamellipodia with a spread-out cell body. In contrast, the NPC43 cell extended filopodia-like protrusions with an elongated cell body to interact with the surrounding microenvironment, which made it easier for the cell to squeeze into the 10 μm wide trench. These cell morphologies were representative of the majority of the cells (over 30 cells of each type) imaged by scanning electron microscopy after three independent runs under the same conditions. Fig. 4(b) shows that on the two-layer platforms, the NP460 cells had a 10% probability of squeezing into the 10 μm wide trenches, which was not possible on the one-layer platforms. On the other hand, the NPC43 cells had a much higher probability of squeezing into the narrow trenches, at 70%. The effects of platform stiffness were studied on two-layer scaffold platforms with PDMS base:agent mix ratios at 5:1 and 10:1. As shown in Fig. 4(b), different platform stiffnesses had little effect on the probability of NP460 cells, but the probability was 4% higher for NPC43 cells on stiffer platforms. NP460 and NPC43 cell separation is related to their different cell morphologies on the patterned platforms. The probability of NPC43 cells squeezing into the 10 μm wide

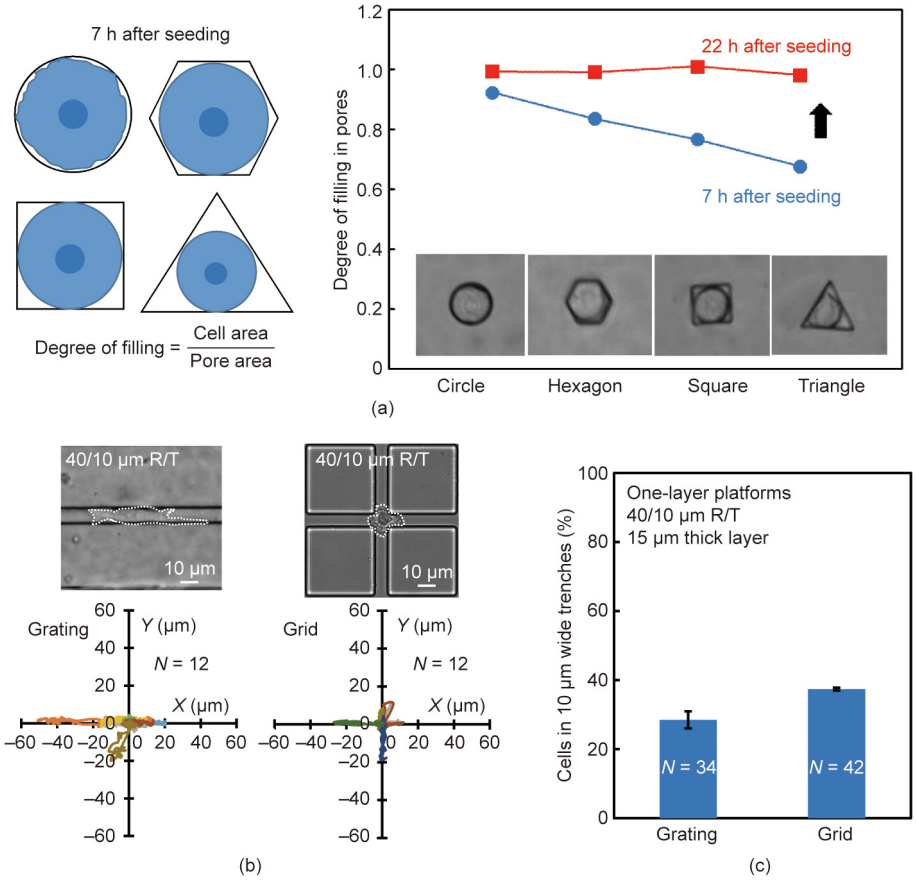

Fig. 3. (a) Degree of filling of NPC43 cells in 15 μm deep pores with different shapes but the same area. (b) Migration trajectories and (c) probability of NPC43 cells migrating into 10 μm wide trenches with a 40/10 μm R/T grating and grid. Depth of trenches was 15 μm and PDMS base:agent mix ratio was 5:1.

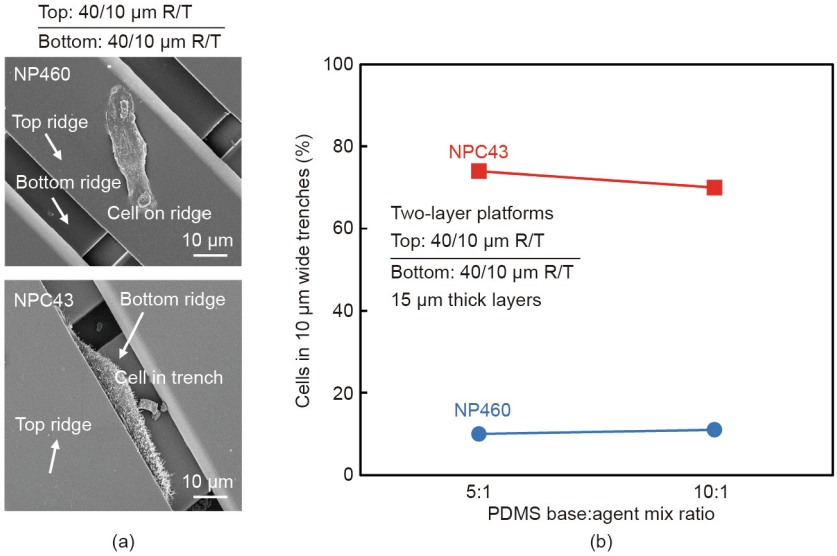

Fig. 4. (a) Micrographs of NP460 cell on the top ridge and NPC43 cell in the top trenches on two-layer scaffold platforms with a top and bottom layer of 40/10 μm R/T (representative of over 30 cells of each type from three independent runs). (b) Probabilities of NP460 and NPC43 cells in 10 μm wide top trenches on two-layer scaffold platforms with different stiffnesses (error bars within 1%). The thickness of each layer was 15 μm.

trenches was 64% higher than that of NP460 cells when a two-layer scaffold platform with 40/10 μm R/T gratings was used on the stiffer 5:1 PDMS base:agent mix ratio.

3.2.2. Effects of bottom layer structure

In order to further increase the cell-separation efficiency, the bottom-layer pattern was changed from a grating to a grid and

the top-layer grating was placed perpendicular to the bottom layer, as shown in Fig. 5(a). As the grid pattern provided more contact area at the intersections, more NPC43 cells could get into the narrow trenches. The platforms were made of a 5:1 PDMS base:agent mix ratio with a 40/10 μm R/T grating on the top layer and a 40/10 μm R/T grating or grid on the bottom layer, both 15 μm deep. Fig. 5(b) shows that changing the bottom-layer pattern from a grating to a grid had no effect on the NP460 cells, but led to a 3% increase in the probability of the NPC43 cells squeezing into the 10 μm wide trenches

The grid pattern not only provided more contact area at the intersections, but also allowed more filopodia-like protrusions of the NPC43 cells to come into contact with the trenches on the bottom layer, which resulted in more NPC43 cells squeezing into the 10 μm wide trenches. To study the effects of cell contact with the bottom-layer trenches on NP460 and NPC43 cell separation, two-layer scaffold platforms with a 40/10 μm R/T grating on the top layer and with the width of the bottom-layer ridges increasing from 10, 20, 40, 80 to 160 μm were fabricated, as shown in Fig. 6(a). The gradually increased distance between the 10 μm wide bottom-layer trenches made it more difficult for the NPC43 cell protrusions to come into contact with the bottom-layer trenches. Fig. 6(b) shows that the probability for NPC43 cells to squeeze into the narrow trenches decreased with increasing ridge width, most likely due to the reduced cell contact with the bottom-layer trenches.

Micrographs of NPC43 cells on two-layer scaffold platforms with bottom-layer grids of 20/10 and 40/10 μm R/T are shown in Fig. 6(c). When the ridge width was larger, the separation between the 10 μm wide trenches was also larger, and the NPC43 cells had to extend longer protrusions in order to reach the trenches in the bottom layer. Fig. 6(d) shows that with denser bottom grids, there was little difference in the probability of the NP460 cells getting into the narrow trenches, while the probability of the NPC43 cells squeezing into the 10 μm wide trenches increased by 8%.

Cell polarization shape was quantified by fitting a cell into an ellipse and measuring its long and short axes. Typically, a more elongated cell shape could fit into a narrower trench. The short axis lengths of the NP460 and NPC43 cells on two-layer scaffold platforms with a bottom-layer grid of 20/10 μm R/T are compared in Fig. 6(e). The figure shows that the NP460 cells were more spread out on the platforms, with an average short axis length of 22 μm, while the NPC43 cells were more elongated, with a reduced average short axis length of 12 μm. The more elongated shape and smaller size of the NPC43 cells, compared with those of the NP460 cells, could have made it easier for them to squeeze into the 10 μm wide trenches in the 3D platforms; thus, there was a 75% higher probability of NPC43 cells squeezing into the 10 μm wide trenches, compared with NP460 cells, when a 20/10 μm R/T grid pattern was used in the bottom layer.

3.3. NP460 and NPC43 cells co-cultured on two-layer scaffold platforms

Thus far, the NP460 and NPC43 cell-separation probabilities were based on seeding the two kinds of cells separately on the platforms. Next, NP460 and NPC43 cells were co-cultured on the optimized two-layer scaffold platforms with a 20/10 μm R/T grid on the bottom layer. Both the NP460 and NPC43 cells were transfected with differently colored fluorescent proteins so that they could be distinguished under fluorescent imaging; NP460 cells were green and NPC43 cells were red.

As mentioned above, cells that divided, died, or came into contact with other cells were excluded from the analysis. Thus, a cell density of 1.1×10^5 cells·mL^{-1} and a suspension volume of 2 mL were found to be optimal in this study. When NP460 and NPC43 cells were co-cultured, the same cell density was used for each cell. The total cell density of 2.2×10^5 cells·mL^{-1} was much lower in comparison with the number of cells available for a nasopharyngeal carcinoma tumor in its early stage [49]. Therefore, the proposed platform could be used for early diagnosis of NPC when the NPC43 cell density is low. The platform can also be scaled up to separate a large number of cells by using a platform with larger area.

Fig. 7(a) shows the fluorescent and bright-field images of co-cultured NP460 and NPC43 cells on the two-layer platforms with 20/10 and 40/10 μm R/T grids on the bottom layer. After culturing the cells in the incubator for 6 h, live fluorescent images were taken, followed by continuous cell imaging under a bright field for 15 h. Fig. 7(b) shows that the NP460 and NPC43 cells had 10% and 84% probability, respectively, of squeezing into the 10 μm wide trenches on the two-layer scaffold platforms with the 20/10 μm R/T grids. Therefore, a separation probability of 74% was obtained when both the NP460 and NPC43 cells were co-cultured on such platforms. The denser 20/10 μm R/T grids were more efficient for cell separation, as the NPC43 cells had a high probability of 84% of reaching the narrow trenches, compared with

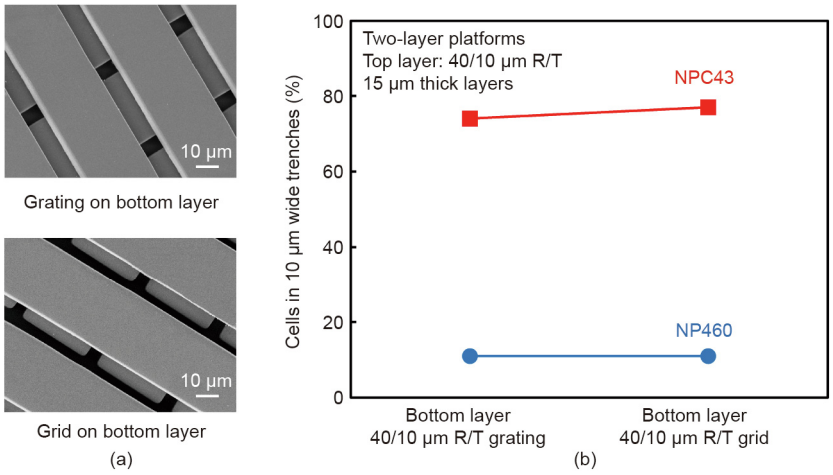

Fig. 5. (a) Micrographs of two-layer platforms with 40/10 μm R/T gratings and grids in the bottom layer. (b) Probabilities of NP460 and NPC43 cells reaching the 10 μm wide trenches on the two-layer platforms with 40/10 μm R/T gratings and grids on the bottom layer (error bars within 1%). The depth of each layer was 15 μm and the PDMS base: agent mix ratio was 5:1.

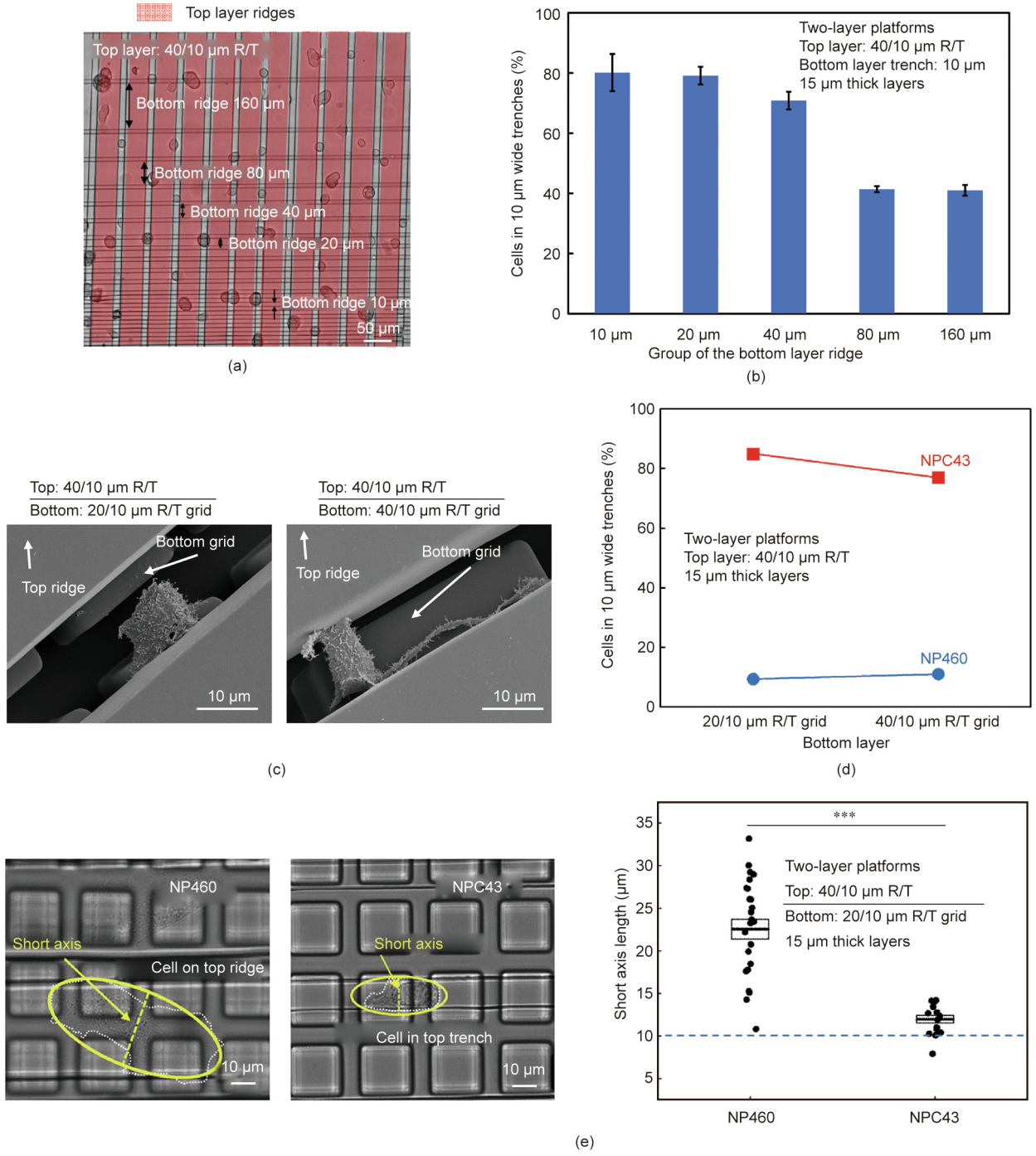

Fig. 6. (a) Micrograph and (b) probabilities of NPC43 cells on two-layer platforms with bottom-layer ridges of 10, 20, 40, 80, and 160 μm widths. All trenches were 10 μm wide. (c) Micrographs of an NPC43 cell with extended protrusions to reach the bottom-layer grid trenches on a two-layer platform. (d) Probabilities of NP460 and NPC43 cells reaching the 10 μm wide top trenches on two-layer platforms with 20/10 and 40/10 μm R/T grids on the bottom layer (error bars within 1%). (e) Short axis lengths of NP460 and NPC43 cells on two-layer platforms with a 20/10 μm R/T grid on the bottom layer. The thickness of each layer was 15 μm and the PDMS base:agent mix ratio was 5:1 ($N > 30$; ***: $p < 0.001$).

a lower probability of 73% on platforms with 40/10 μm R/T grids on the bottom layer.

After separation, the NPC43 cells could be preserved and collected through an exit port in the microfluidic platform near the bottom, while the NP460 cells could be channeled through another exit port on the top layer. Alternatively, laser microdissection technology [50] could be used to precisely cut off the top part of the platform and separate the platform into two halves. After the separation, the NP460 cells could be harvested from the top half and the NPC43 cells could be collected from the bottom half of the platform.

3.4. Effects of NPC cell motility on cell separation

The motility of NPC43 cells can influence cell movement in the 3D ECM, as cancer cells often have different motility during tumor progression [51–53]. The ACM obtained from the exosomes of a fibroblast have been shown to enhance the motility and metastasis

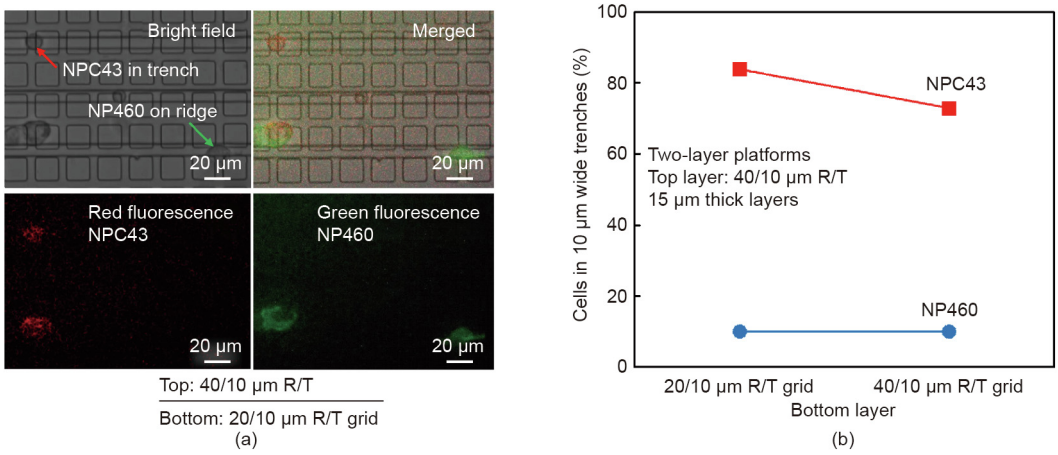

Fig. 7. (a) Bright-field and fluorescent micrographs of NP460 and NPC43 cells co-cultured on two-layer platforms with a 20/10 μm R/T grid on the bottom layer. NP460 cells were transfected with green fluorescent protein and NPC43 cells were transfected with red fluorescent protein. (b) Separation probability of co-cultured NP460 and NPC43 cells on two-layer platforms with 20/10 and 40/10 μm R/T grids on the bottom layer (error bars within 1%). The thickness of each layer was 15 μm and the PDMS base:agent mix ratio was 5:1.

of certain cancer cells [54,55]. In this study, ACM was added to the culture medium of NPC43 cells to examine the changes in motility and their effects on the separation efficiency of NPC43 cells from NP460 cells.

The migration speed of the NPC43 cells was faster on one-layer platforms with 40/10 μm R/T when the NPC43 cell-culturing medium was mixed with ACM in a volume ratio of 1:1, as shown in Fig. 8(a); this demonstrated that the ACM could enhance the motility of the NPC43 cells. It has been suggested that the tetraspanins Cd81 of the exosomes contained in ACM can promote the motility of cancer cells via Wnt/planar cell polarity signaling [54]. The changes in cell shape, as indicated by the cell aspect ratio, were monitored over time after the ACM was added, since the cells had a different probability of getting into the narrow trenches after the cell shape changed. As shown in Fig. 8(b), the NPC43 cells cultured with ACM showed a larger aspect ratio and were more elongated on the one-layer platforms with 40/10 μm R/T and a 5:1 PDMS base:agent mix ratio. Fig. 8(c) shows that 34% of the NPC cells were able to squeeze into the 10 μm wide trenches on the top layer, and then moved further into the bottom-layer grid. Thus

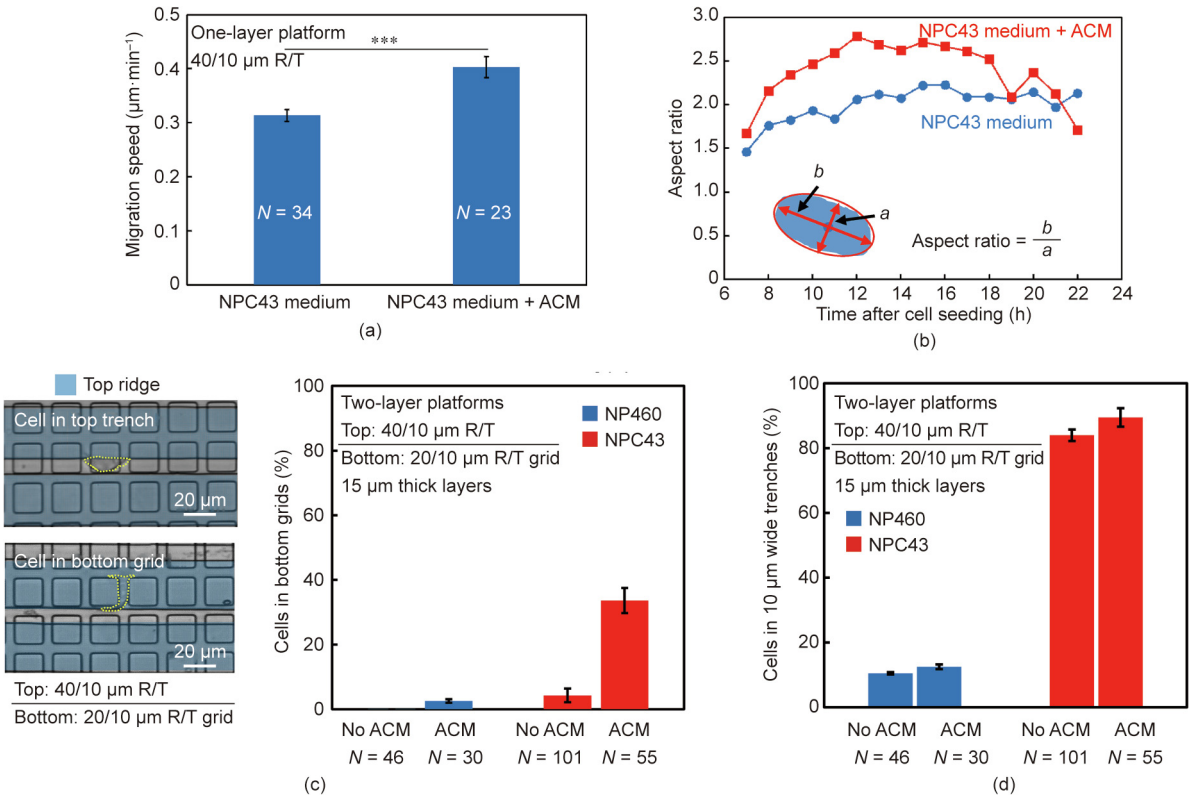

Fig. 8. (a) Migration speed and (b) aspect ratio of NPC43 cells stimulated by ACM on one-layer platforms with 10 μm wide trenches (***: $p < 0.001$). (c) Probability of NPC43 cells reaching a 20/10 μm R/T bottom grid on two-layer platforms stimulated by ACM. (d) Probabilities of NP460 and NPC43 cell migration stimulated by ACM in trenches on two-layer platforms with a 20/10 μm R/T bottom grid. The thickness of each layer was 15 μm and the PDMS base:agent mix ratio was 5:1.

there was a greater than eight-fold increase in the probability of NPC43 cells reaching the bottom layer grid when they were cultured with added ACM. Therefore, these results show that the ACM effectively stimulated the NPC43 cells to modify their motility and morphology, which allowed the NPC43 cells to squeeze through the narrow trenches and move into the bottom-layer grid in 3D platforms.

NPC43 cells with ACM were co-cultured with NP460 cells on two-layer scaffold platforms with a 20/10 μm R/T grid on the bottom layer and a 5:1 PDMS base:agent mix ratio. The results in Fig. 8(d) show a 5% increase of the probability of NPC43 cells squeezing into the 10 μm trenches when ACM was added. The addition of ACM increased the NPC43 cell speed and cell elongation, making it easier for the cells to move through the 10 μm wide trenches and further into the bottom-layer grid. However, the presence of ACM showed little influence on the movement of the NP460 cells into the top-layer trenches or the bottom-layer grid. Therefore, the addition of ACM in the culture medium helped to further separate the NPC43 cells from the NP460 cells in the bottom-layer grid. Using multi-layer platforms, a higher cell-separation efficiency could be achieved for more active cancer cells.

4. Conclusion

Cell separation between normal and cancer cells is critical in cancer diagnostics, treatment, and drug development. Details of NPC cell migration behaviors have not been reported previously, due to the difficulty of establishing stable EBV-positive cell lines. In this work, 3D scaffold platforms were developed to separate NPC43 cells from NP460 cells based on the platform properties. Design parameters including platform stiffness, grating or grid pattern layouts, number of layers, and density of grid patterns were used to optimize the platform design in order to achieve the highest separation efficiency.

Using two-layer scaffold platforms with a 20/10 μm R/T grid on the bottom layer resulted in an 89% separation efficiency of NPC43 cells from NP460 cells in the top-layer 10 μm wide trenches. When NPC43 cells were granted enhanced motility through ACM stimulation, a 93% separation probability was obtained in the bottom-layer grid. As NPC cells are highly invasive and metastatic, it is important to be able to separate these cancer cells from normal cells. The results illustrated in Fig. 8 show that the NPC43 cells had higher motility and deformability after ACM stimulation, and the separation efficiency was improved. Based on this principle, the separation of other types of cancer cells from normal cells with different motilities and deformability will also be feasible. In our previous work [56], we demonstrated the capability of screening various types of cancer cells on platforms with appropriate topographical designs. Further studies will be conducted to investigate the optimal platform layouts and characteristics that can be used to separate other cancer cell lines.

Acknowledgments

This work was supported by the Center for Biosystems, Neuroscience, and Nanotechnology (CBNN) of City University of Hong Kong (9360148 and 9380062) and the University Grants Council of Hong Kong (GRF projects: 11247716, 11218017, 11213018, and 11212519; CRF project: C1013-15G). The authors would like to thank Prof. S.W. Tsao and C.M. Tsang from the University of Hong Kong for providing the NP460 and NPC43 cells, and Dr. L. Zhang from City University of Hong Kong for providing active conditioned medium.

Compliance with ethics guidelines

W.G. Zhang, Z.Y. Liu, and S.W. Pang declare that they have no conflict of interest or financial conflicts to disclose.

References

[1] Gossett DR, Weaver WM, Mach AJ, Hur SC, Tse HTK, Lee W, et al. Label-free cell separation and sorting in microfluidic systems. Anal Bioanal Chem 2010;397(8):3249–67.
[2] Fiddler M. Fetal cell based prenatal diagnosis: perspectives on the present and future. J Clin Med 2014;3(3):972–85.
[3] Blainey PC, Quake SR. Dissecting genomic diversity, one cell at a time. Nat Methods 2014;11(1):19–21.
[4] Schor SL, Schor AM. Phenotypic and genetic alterations in mammary stroma: implications for tumour progression. Breast Cancer Res 2001;3(6):373–9.
[5] Guo KT, SchÄfer R, Paul A, Gerber A, Ziemer G, Wendel HP. A new technique for the isolation and surface immobilization of mesenchymal stem cells from whole bone marrow using high-specific DNA aptamers. Stem Cells 2006;24(10):2220–31.
[6] Cho SH, Chen CH, Tsai FS, Godin JM, Lo YH. Human mammalian cell sorting using a highly integrated micro-fabricated fluorescence-activated cell sorter (μFACS). Lab Chip 2010;10(12):1567–73.
[7] Pasut A, Oleynik P, Rudnicki MA. Isolation of muscle stem cells by fluorescence activated cell sorting cytometry. Methods Mol Biol 2012;798:53–64.
[8] Schulz KR, Danna EA, Krutzik PO, Nolan GP. Single-cell phospho-protein analysis by flow cytometry. Curr Protoc Immunol 2012;96(1):8.17.1-20.
[9] Wu M, Singh AK. Single-cell protein analysis. Curr Opin Biotechnol 2012;23(1):83–8.
[10] Miltenyi S, Müller W, Weichel W, Radbruch A. High gradient magnetic cell separation with MACS. Cytometry 1990;11(2):231–8.
[11] Allan AL, Vantyghem SA, Tuck AB, Chambers AF, Chin-Yee IH, Keeney M. Detection and quantification of circulating tumor cells in mouse models of human breast cancer using immunomagnetic enrichment and multiparameter flow cytometry. Cytometry A 2005;65(1):4–14.
[12] Hejazian M, Li W, Nguyen NT. Lab on a chip for continuous-flow magnetic cell separation. Lab Chip 2015;15(4):959–70.
[13] Holt LM, Olsen ML. Novel applications of magnetic cell sorting to analyze cell-type specific gene and protein expression in the central nervous system. PLoS ONE 2016;11(2):e0150290.
[14] Citri A, Pang ZP, Südhof TC, Wernig M, Malenka RC. Comprehensive qPCR profiling of gene expression in single neuronal cells. Nat Protoc 2011;7(1):118–27.
[15] Paiè P, Zandrini T, Vázquez RM, Osellame R, Bragheri F. Particle manipulation by optical forces in microfluidic devices. Micromachines 2018;9(5):200.
[16] Eberwine J, Yeh H, Miyashiro K, Cao Y, Nair S, Finnell R, et al. Analysis of gene expression in single live neurons. Proc Natl Acad Sci USA 1992;89(7):3010–4.
[17] Yousuff CM, Ho ETW, Hussain KI, Hamid NHB. Microfluidic platform for cell isolation and manipulation based on cell properties. Micromachines 2017;8(1):15.
[18] Tai CH, Hsiung SK, Chen CY, Tsai ML, Lee GB. Automatic microfluidic platform for cell separation and nucleus collection. Biomed Microdevices 2007;9(4):533–43.
[19] Yun H, Kim K, Lee WG. Cell manipulation in microfluidics. Biofabrication 2013;5(2):022001.
[20] Shields IV CW, Reyes CD, López GP. Microfluidic cell sorting: a review of the advances in the separation of cells from debulking to rare cell isolation. Lab Chip 2015;15(5):1230–49.
[21] Ji HM, Samper V, Chen Y, Heng CK, Lim TM, Yobas L. Silicon-based microfilters for whole blood cell separation. Biomed Microdevices 2008;10(2):251–7.
[22] Huang LR, Cox EC, Austin RH, Sturm JC. Continuous particle separation through deterministic lateral displacement. Science 2004;304(5673):987–90.
[23] Kuntaegowdanahalli SS, Bhagat AAS, Kumar G, Papautsky I. Inertial microfluidics for continuous particle separation in spiral microchannels. Lab Chip 2009;9(20):2973–80.
[24] Zheng S, Lin H, Liu JQ, Balic M, Datar R, Cote RJ, et al. Membrane microfilter device for selective capture, electrolysis and genomic analysis of human circulating tumor cells. J Chromatogr A 2007;1162(2):154–61.
[25] Takagi J, Yamada M, Yasuda M, Seki M. Continuous particle separation in a microchannel having asymmetrically arranged multiple branches. Lab Chip 2005;5(7):778–84.
[26] Yamada M, Kano K, Tsuda Y, Kobayashi J, Yamato M, Seki M, et al. Microfluidic devices for size-dependent separation of liver cells. Biomed Microdevices 2007;9(5):637–45.
[27] Kuo JS, Zhao Y, Schiro PG, Ng L, Lim DSW, Shelby JP, et al. Deformability considerations in filtration of biological cells. Lab Chip 2010;10(7):837–42.
[28] Mohamed H, Turner JN, Caggana M. Biochip for separating fetal cells from maternal circulation. J Chromatogr A 2007;1162(2):187–92.
[29] Hsu CH, Di Carlo D, Chen C, Irimia D, Toner M. Microvortex for focusing, guiding and sorting of particles. Lab Chip 2008;8(12):2128–34.
[30] Chen DF, Du H, Li WH. A 3D paired microelectrode array for accumulation and separation of microparticles. J Micromech Microeng 2006;16(7):1162.

[31] Cui HH, Voldman J, He XF, Lim KM. Separation of particles by pulsed dielectrophoresis. Lab Chip 2009;9(16):2306–12.
[32] MacDonald MP, Spalding GC, Dholakia K. Microfluidic sorting in an optical lattice. Nature 2003;426(6965):421–4.
[33] Milne G, Rhodes D, MacDonald M, Dholakia K. Fractionation of polydisperse colloid with acousto-optically generated potential energy landscapes. Opt Lett 2007;32(9):1144–6.
[34] McFaul SM, Lin BK, Ma H. Cell separation based on size and deformability using microfluidic funnel ratchets. Lab Chip 2012;12(13):2369–76.
[35] Preira P, Grandné V, Forel JM, Gabriele S, Camara M, Theodoly O. Passive circulating cell sorting by deformability using a microfluidic gradual filter. Lab Chip 2013;13(1):161–70.
[36] Lu X, Martin A, Soto F, Angsantikul P, Li J, Chen C, et al. Parallel label-free isolation of cancer cells using arrays of acoustic microstreaming traps. Adv Mater Technol 2019;4(2):1800374.
[37] Tang QY, Tong WY, Shi J, Shi P, Lam YW, Pang SW. Influence of engineered surface on cell directionality and motility. Biofabrication 2014;6(1):015011.
[38] Zhou SF, Gopalakrishnan S, Xu YH, Yang J, Lam YW, Pang SW. A unidirectional cell switching gate by engineering grating length and bending angle. PLoS ONE 2016;11(1):e0147801.
[39] Wei WI, Sham JST. Nasopharyngeal carcinoma. Lancet 2005;365 (9476):2041–54.
[40] Chan KCA, Hung ECW, Woo JKS, Chan PKS, Leung SF, Lai FPT, et al. Early detection of nasopharyngeal carcinoma by plasma Epstein–Barr virus DNA analysis in a surveillance program. Cancer 2013;119(10):1838–44.
[41] Siva Sankar P, Mat MFC, Muniandy K, Xiang BLS, Ling PS, Hoe SLL, et al. Modeling nasopharyngeal carcinoma in three dimensions. Oncol Lett 2017;13 (4):2034–44.
[42] Yip YL, Lin W, Deng W, Jia L, Lo KW, Busson P, et al. Establishment of a nasopharyngeal carcinoma cell line capable of undergoing lytic Epstein–Barr virus reactivation. Lab Invest 2018;98(8):1093–104.
[43] Dittmer DP, Hilscher CJ, Gulley ML, Yang EV, Chen M, Glaser R. Multiple pathways for Epstein–Barr virus episome loss from nasopharyngeal carcinoma. Int J Cancer 2008;123(9):2105–12.
[44] Lin W, Yip YL, Jia L, Deng W, Zheng H, Dai W, et al. Establishment and characterization of new tumor xenografts and cancer cell lines from EBV-positive nasopharyngeal carcinoma. Nat Commun 2018;9(1):4663.
[45] Wang Y, Wang G, Luo X, Qiu J, Tang C. Substrate stiffness regulates the proliferation, migration, and differentiation of epidermal cells. Burns 2012;38 (3):414–20.
[46] Bangasser BL, Shamsan GA, Chan CE, Opoku KN, Tüzel E, Schlichtmann BW, et al. Shifting the optimal stiffness for cell migration. Nat Commun 2017;8 (1):15313.
[47] Pathak A, Kumar S. Independent regulation of tumor cell migration by matrix stiffness and confinement. Proc Natl Acad Sci USA 2012;109(26):10334–9.
[48] Zhong Y, Ji B. Impact of cell shape on cell migration behavior on elastic substrate. Biofabrication 2013;5(1):015011.
[49] Huang L, Chua MLK. Surgery as an alternative to radiotherapy in early-stage nasopharyngeal carcinoma: innovation at the expense of uncertainty. Cancer Commun 2020;40(2–3):119–21.
[50] Zhao L, Lu YT, Li F, Wu K, Hou S, Yu J, et al. High-purity prostate circulating tumor cell isolation by a polymer nanofiber-embedded microchip for whole exome sequencing. Adv Mater 2013;25(21):2897–902.
[51] van Zijl F, Krupitza G, Mikulits W. Initial steps of metastasis: cell invasion and endothelial transmigration. Mutat Res 2011;728(1–2):23–34.
[52] Bange J, Prechtl D, Cheburkin Y, Specht K, Harbeck N, Schmitt M, et al. Cancer progression and tumor cell motility are associated with the FGFR4 Arg388 allele. Cancer Res 2002;62(3):840–7.
[53] Olson MF, Sahai E. The actin cytoskeleton in cancer cell motility. Clin Exp Metastasis 2009;26(4):273–87.
[54] Luga V, Zhang L, Viloria-Petit AM, Ogunjimi AA, Inanlou MR, Chiu E, et al. Exosomes mediate stromal mobilization of autocrine Wnt–PCP signaling in breast cancer cell migration. Cell 2012;151(7):1542–56.
[55] Zhang L, Luga V, Armitage SK, Musiol M, Won A, Yip CM, et al. A lateral signalling pathway coordinates shape volatility during cell migration. Nat Commun 2016;7(1):11714.
[56] Zhou SF, Gopalakrishnan S, Xu YH, To SKY, Wong AST, Pang SW, et al. Substrates with patterned topography reveal metastasis of human cancer cells. Biomed Mater 2017;12(5):055001.